Supporting Information

Wörmer et al. 10.1073/pnas.1405237111

SI Results

Importance of Artificial Matrix in LDI FTICR-MS Analysis of Sediment Samples. The application of artificial matrix did only slightly improve the intensity of spectra in one single case (Fig. S4). This may be related to the characteristics of the analyzed samples. Marine sediments contain abundant Na^+ and a variety of constituents that may act as natural, ionization-facilitating matrix due to strong absorption in the laser emission wavelength. As the effect of alpha-cyano-4-hydroxycinnamic acid (HCCA) is limited, and to avoid negative effects associated with sample preparation (e.g., diffusion of the matrix through the sediment sample leading to lipid solubilization and negatively affecting spatial resolution), we chose to perform our experiments without artificial matrix. The recently proposed application of dry matrix for detection of lipids (e.g., ref. 1) was not evaluated because LDI measurements were already satisfactory, and dry matrix additions would have counteracted our aim of developing a method with minimal sample manipulation.

Modeling Spatial Patterns with Principal Coordinates of Neighbor Matrices (PCNM) Analysis. The dataset generated in this study may be treated as a 2D spatial map of a response variable (CCaT) and the distances between measurements may, in themselves, reveal informative patterns. As noted by Dray et al. (2), spatial structure in a response variable may be (*i*) induced by spatially structured environmental processes, (*ii*) the result of spatially autocorrelated biotic processes, or (*iii*) a combination of the two. Thus, spatial analyses can provide an initial bearing on potentially important environmental or biotic processes that were not directly measured. Intersample distances, as represented by a square, symmetrical, Euclidean distance matrix derived from each point's coordinates, can be mapped to variables, which may be used in regression-type analyses by using principal components of neighbor matrices (3). Using the pcnm() and rda() functions in the R package (4), vegan (5), we applied this flexible method, closely related to spatial autocorrelation structure functions, to decompose the spatial structure in our data across multiple scales. Following the vegan implementation's default, all distances greater than an automatically determined truncation threshold of 0.07 units (the minimum distance at which all points are connected) were set to four times this threshold distance.

A total of 1,607 PCNM vectors with positive eigenvalues were found which, when used as explanatory variables in a partial redundancy analysis [pRDA; partialling out the effect of any spatial trend in the data (cf. ref. 6)] constrained ∼56% of the variation in the response variable (*P* value after 200 permutations = 0.005). Due to the large number of PCNM vectors, the adjusted R^2 was considerably lower, at ∼0.07. A number of PCNM variables with the greatest explanatory power in the pRDA model are illustrated in Fig. S6. Presence of coarse- to fine-grained (e.g., PCNM 51 to PCNM 1,214, respectively) spatial patterns illustrate the diversity of scales that are redundant with the observed data variability.

As an exploratory exercise, PCNMs were sequentially added to a trivial pRDA model (i.e., void of explanatory variables) in an order determined by their absolute canonical coefficients (greatest to least) along the constrained axis obtained in the full pRDA model, described above. After the addition of 685 PCNMs, the adjusted R^2 begins to fall from a maximum of ∼0.349 (unadjusted R^2 ∼0.495). All models had false discovery rate-corrected *P* values (determined by 200 permutations) below 0.05 (median: 0.005031, lowest possible value at 200 permutations: 0.005). It must be noted, however, that a large number of data points often leads to greater significance of small, and potentially unimportant, effects. Repeated and independent confirmation across related studies will clarify which effects and spatial patterns are sustained and noteworthy. At this stage, we opt for this approach rather than attempting automatic variable selection (as used by ref. 6). Indeed, more work is needed to guide appropriate use of such spatial methods in high-resolution, microscale datasets; however, their potential is considerable.

Calculation of Sedimentation Rates for Sapropel 1 at Location GeoB 15103. The unoxidized layer of sapropel 1 at our station is about 19 cm thick according to element concentrations obtained by XRF scanning (7, 8) (Fig. S9) and thus slightly thicker than most sapropel 1 layers (e.g., ref. 9). The pore water profile of Mn clearly indicates that the postdepositional oxidation (burn down) is still ongoing. The formation of sapropel 1 in the eastern Mediterranean is considered a basinwide synchronous event (10), and the unoxidized sapropel has been described to cover an average of 3,000 y of sediment deposition (e.g., ref. 11). Assuming a continuous deposition, this translates into a linear sedimentation rate of about 6.3 cm ky^{-1}. This value is in general agreement with a sedimentation rate of 6.6 cm ky^{-1} for the interval between 6.31 and 7.60 ky [23 and 32 cm below seafloor (cmbsf); corresponding to the upper section of sapropel 1] derived from the age determination by Paterne [data deposited in Pangaea database, www.pangaea.de (doi: 10.1594/PANGAEA.407609)] for sediment core MD84-641 taken at immediate proximity to our study site.

Estimation of Analytical Uncertainty. Analytical uncertainty of downcore CCaT profiles was obtained from a ground sample (see next section for details) smeared on a sample holder. Spatially resolved analysis was carried out and obtained spectra were processed as described for the unaltered sediment section, i.e., individual measurements from each horizon were averaged to a single data point. The resulting 122 data points were used to estimate analytical uncertainty as two SDs. This reported uncertainty probably reflects both true analytical uncertainty and incomplete homogenization.

SI Materials and Methods

Test Sample for Detection of GDGTs by LDI FT-ICRMS. A mixture of Mediterranean sapropels 1, 3, and 5 taken from core GeoB 15103–1 in the eastern Mediterranean Sea (33°02′, 32°38′; ref. 12) was used. When needed, grinding was carried out at −196 °C, using a Retsch Cryomill with three cycles consisting of precooling (5 min, 5 impacts/s) and milling (2 min, 25 impacts/s).

Analysis of GDGTs by LDI FT-ICRMS. Each single LDI FT-ICRMS scan was recorded using the ions generated by 1,000 laser shots. The laser was running at 1 KHz (50% laser power) and the ions were accumulated externally in a hexapole before being transferred into the ion cyclotron resonance cell for a single scan. Data sizes of one megaword were acquired for the mass range $700 < m/z < 3{,}000$ followed by a single zero filling and a sine apodization. External calibration was done with a standard peptide mixture (Bruker Daltonics) in MALDI mode followed by an internal lock mass calibration using the *m/z* value 1,314.22636 of the GDGT-5 Na^+-ion.

Initial interpretation of mass spectra was performed with Bruker DataAnalysis 4.1. Raw data were then exported and processed with MATLAB by selecting *m/z* values corresponding to the different GDGT species (window = 3 mDa) and by applying

a signal-to-noise ratio (SNR) threshold of 5. The statistical programming language and environment R was used for PCNM and pRDA (see *Modeling Spatial Patterns with PCNMS Analysis* for more detail), Sigma Plot 11.0 for ANOVA tests and running average calculation and PAST (Paleontological Statistics) version 2.17c (13) for spectral analysis and band pass filtering. The REDFIT procedure was used for spectral analysis, as it allows distinguishing relevant signals from theoretical red-noise background originating from first-order autoregressive processes (14). By scaling up the theoretical red noise, a false alarm level can be established. We set this false alarm level to 99%. For bandpass filtering, data were normalized by subtraction of the mean value.

Sample Extraction and Analysis by HPLC/APCI-MS. Samples were extracted by ultrasonication into a solvent mixture (v:v) of methanol (MeOH), dichloromethane (DCM), and aqueous buffer (2:1:0.8). A phosphate buffer (8.7 g L^{-1} KH_2PO_4, pH 7.4) was used for the first two steps, and a trichloroacetic acid buffer (50 g L^{-1}, pH 2) for the final two steps. Supernatants were pooled in a separation funnel and DCM and water were added to allow optimal phase separation. After transferring the organic phase, the aqueous phase was extracted three more times with DCM. Pooled organic layers were then washed three times with deionized milliQ water. The final extract was gently evaporated under N_2 flow and stored at –20 °C.

Chromatographic separation was achieved on a Dionex Ultimate 3000RS system connected to a maXis quadrupole time-of-flight mass spectrometer (Qtof-MS; Bruker Daltonics) equipped with an APCI II ion source. Aliquots (10 µl) dissolved in n-hexane: isopropanol (99.5:0.5, v:v), were injected on two coupled Acquity BEH Amide columns (2.1 × 150 mm, 1.7 µm; Waters) maintained at 50 °C, using the published solvent gradient (15). Detection and identification of GDGTs in positive ionization mode was based on exact mass and retention time.

XRF Scanning and Detection of Element Concentrations. Relative intensities of sulfur, manganese, bromine, and silicon from the upper 80 cm of core GeoB15103-1 were obtained in 1-cm resolution using the AVAATECH X-ray fluorescence core scanner II at MARUM and are given in total counts per second.

SI Equations

GDGT ratios were calculated accounting for the abundance of species with different number of rings (Fig. S1; expressed in the equations with [n] indicating the number of cycloalkyl moieties and [5′] designating the regioisomer of compound [5]).

Eq. S1. Correlation between CCaT values obtained by the conventional HPLC/APCI-MS method and the LFI FTICR-MS method in 21 samples from the Mediterranean, Marmara, and Black seas (Fig. 1). This correlation enables SST calculation according to Eq. **S5**.

$$\mathrm{CCaT_{LC}} = -0.017 + 1.056 \times \mathrm{CCaT_{LDI}}.$$

Eq. S2. Definition of the widely used TEX_{86} index for SST calculation (16):

$$\mathrm{TEX_{86}} = \left([2] + [3] + [5']\right) / \left([1] + [2] + [3] + [5']\right).$$

Eq. S3. Definition of the methane index (MI) for detection of enhanced methanotrophic activity (17):

$$\mathrm{MI} = \left([1] + [2] + [3]\right) / \left([1] + [2] + [3] + [5] + [5']\right).$$

Eq. S4. Correlation between MI obtained by the conventional HPLC/APCI-MS method and the LDI FTICR-MS method in 21 samples from the Mediterranean, Marmara, and Black seas (Fig. S5*A*). This correlation was used to calculate the threshold for increased methanotrophy (17) for LDI FTICR-MS measurements (Fig. S8):

$$\mathrm{MI_{LC}} = -0.074 + 0.956 \times \mathrm{MI_{LDI}}.$$

Eq. S5. SST calibration for CCaT values retrieved from the global data set by Kim et al. (18) and Ho et al. (19) (Fig. S5*B*) and used for SST estimations after conversion of the LDI measurements according to Eq. **S1**.

$$\mathrm{SST} = -18.758 + 64.774 \times \mathrm{CCaT_{LC}}.$$

Eq. S6. Correlation between CCaT and TEX_{86} obtained by LFI FTICR-MS in 21 samples from the Mediterranean, Maramara, and Black seas (Fig. S5*C*): This correlation enables SST determination according to Eq. **S7**.

$$\mathrm{TEX_{86}} = -0.542 + 1.832 \times \mathrm{CCaT}.$$

Eq. S7. SST calibration optimized for SST > 15 °C (18), used for the calculation of an SST scale (Fig. 2*B*) from TEX_{86} values that we obtained by conversion of CCaT values according to Eq. **S6**.

$$\mathrm{SST} = 38.6 + 68.4 \times \log(\mathrm{TEX_{86}}).$$

1. Angelini R, Babudri F, Lobasso S, Corcelli A (2010) MALDI-TOF/MS analysis of archaebacterial lipids in lyophilized membranes dry-mixed with 9-aminoacridine. *J Lipid Res* 51(9):2818–2825.
2. Dray S, Legendre P, Peres-Neto PR (2006) Spatial modelling: A comprehensive framework for principal coordinate analysis of neighbour matrices (PCNM). *Ecol Modell* 196(3-4):483–493.
3. Borcard D, Legendre P (2002) All-scale spatial analysis of ecological data by means of principal coordinates of neighbour matrices. *Ecol Modell* 153(1-2):51–68.
4. R Core Team (2013) *R: A Language and Environment for Statistical Computing*. R Foundation for Statistical Computing (Vienna, Austria). http://www.R-project.org/.
5. Oksanen J, et al. (2013) Vegan: Community Ecology Package. http://CRAN.R-project.org/package=vegan.
6. Borcard D, Legendre P, Avois-Jacquet C, Tuomisto H (2004) Dissecting the spatial structure of ecological data at multiple scales. *Ecology* 85(7):1826–1832.
7. Ten Haven HL, De Leeuw JW, Schenk PA, Schenk GT (1987) Geochemistry of Mediterranean sediments. Bromine/organic carbon and uranium/organic carbon ratios as indicators for different sources of input and post-depositional oxidation, respectively. *Org Geochem* 13:255–261.
8. Thomson J, Croudace IW, Rothwell RG (2006) A geochemical application of the ITRAX scanner to a sediment core containing eastern Mediterranean sapropel units. *New Techniques in Sediment Core Analysis*, ed Rothwell RG, Geological Society, London, Special Publications London), Vol 267, pp 65–77.
9. Murat A, Got H (2000) Organic carbon variations of the eastern Mediterranean Holocene sapropel: A key for understanding formation processes. *Palaeogeogr Palaeocl* 158(3-4):241–257.
10. De Lange GJ, et al. (2008) Synchronous basin-wide formation and redox-controlled preservation of a Mediterranean sapropel. *Nat Geosci* 1(9):606–610.
11. Rossignol-Strick M (1999) The Holocene climatic optimum and pollen records of sapropel 1 in the eastern Mediterranean, 9000-6000 BP. *Quat Sci Rev* 18(4-5):515–530.
12. Zabel M (2012) RV METEOR, Cruise Report M84/L1. Biogeochemistry and methane hydrates of the Black Sea; Oceanography of the Mediterranean; Shelf sedimentation and cold water carbonates 2012 (DFG Senatskommission für Ozeanographie, Bremen, Germany).
13. Hammer O, Harper DAT, Ryan PD (2001) PAST: Paleontological statistics software package for education and data analysis. *Palaeontol Electronica* 4(1).
14. Schulz M, Mudelsee M (2002) REDFIT: Estimating red-noise spectra directly from unevenly spaced paleoclimatic time series. *Comput Geosci* 28(3):421–426.
15. Becker KW, Lipp JS, Zhu C, Liu X-L, Hinrichs K-U (2013) An improved method for the analysis of archaeal and bacterial ether core lipids. *Org Geochem* 61:34–44.
16. Schouten S, Hopmans EC, Schefuss E, Damste JSS (2002) Distributional variations in marine crenarchaeotal membrane lipids: A new tool for reconstructing ancient sea water temperatures? *Earth Planet Sci Lett* 204(1-2):265–274.
17. Zhang YG, et al. (2011) Methane Index: A tetraether archaeal lipid biomarker indicator for detecting the instability of marine gas hydrates. *Earth Planet Sci Lett* 307(3-4):525–534.

18. Kim J-H, et al. (2010) New indices and calibrations derived from the distribution of crenarchaeal isoprenoid tetraether lipids: Implications for past sea surface temperature reconstructions. *Geochim Cosmochim Acta* 74(16):4639–4654.

19. Ho SL, et al. (2014) Appraisal of TEX_{86} and TEX_{86}^{L} thermometries in subpolar and polar regions. *Geochim Cosmochim Acta* 131:213–226.

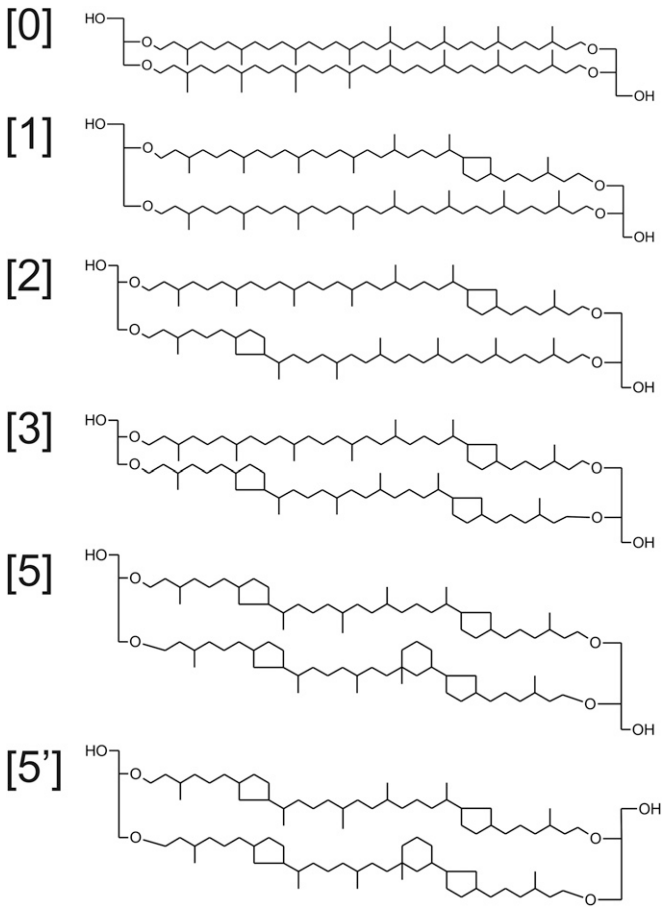

Fig. S1. Core GDGT structures with numbers indicating the number of cycloalkyl moieties in the biphytanyl chains. GDGT-5′ is a regioisomer of GDGT-5 (crenarchaeol).

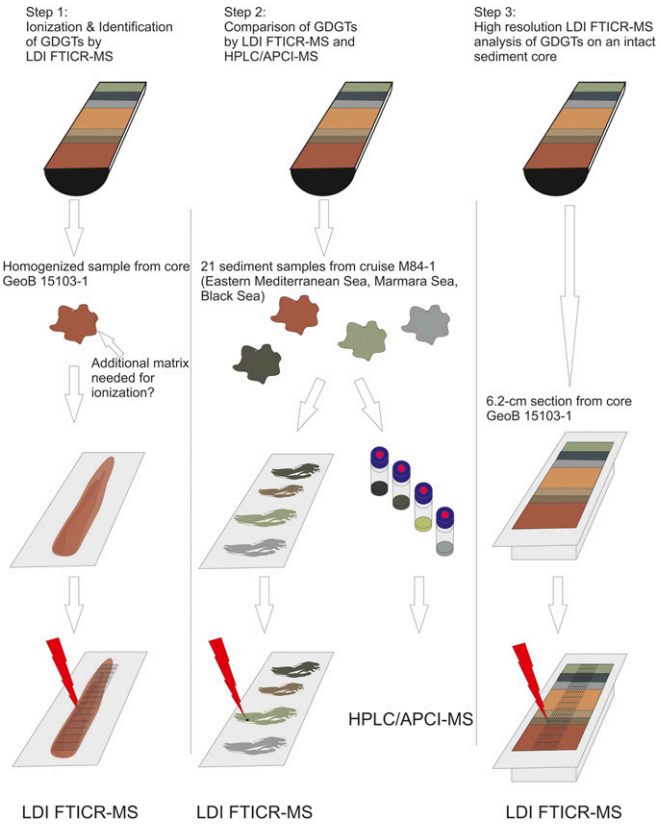

Fig. S2. The three steps of method development and validation performed to test high-resolution analysis of GDGTs by LDI FT-ICRMS.

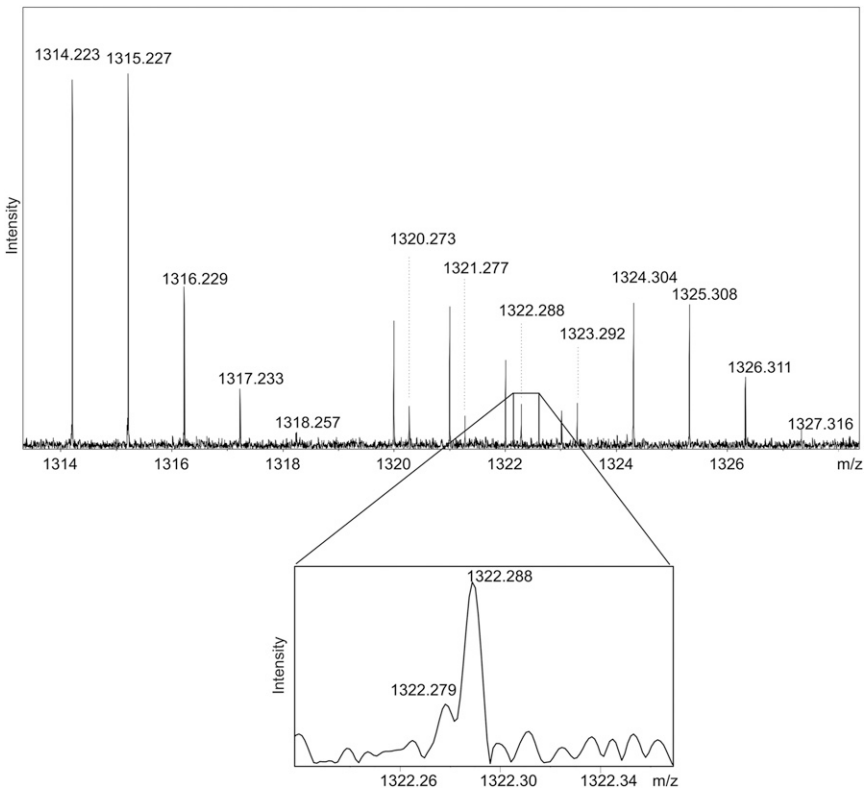

Fig. S3. Na^+ adduct ions of GDGTs detected by LDI FTICR-MS. Enlargement shows the capacity of differentiating GDGT-1 (*m/z* = 1,322.289) and the isotopologue of GDGT-2 containing two ^{13}C (*m/z* = 1,322.280).

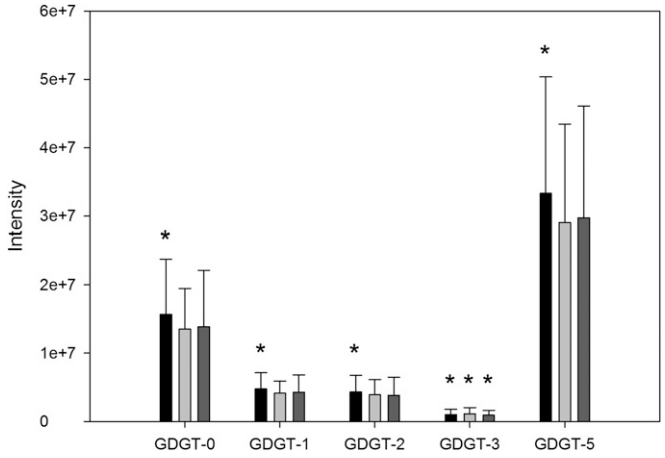

Fig. S4. Intensity of GDGTs in the ground test sample measured by LDI FTICR-MS in presence of HCCA (black bar) and DHB (light gray bar) or absence of matrix (dark gray bar). Mean and SD are shown. (*) Statistical difference observed ($P < 0.005$; ANOVA and Tukey test for pairwise comparison, $n = 1{,}500$).

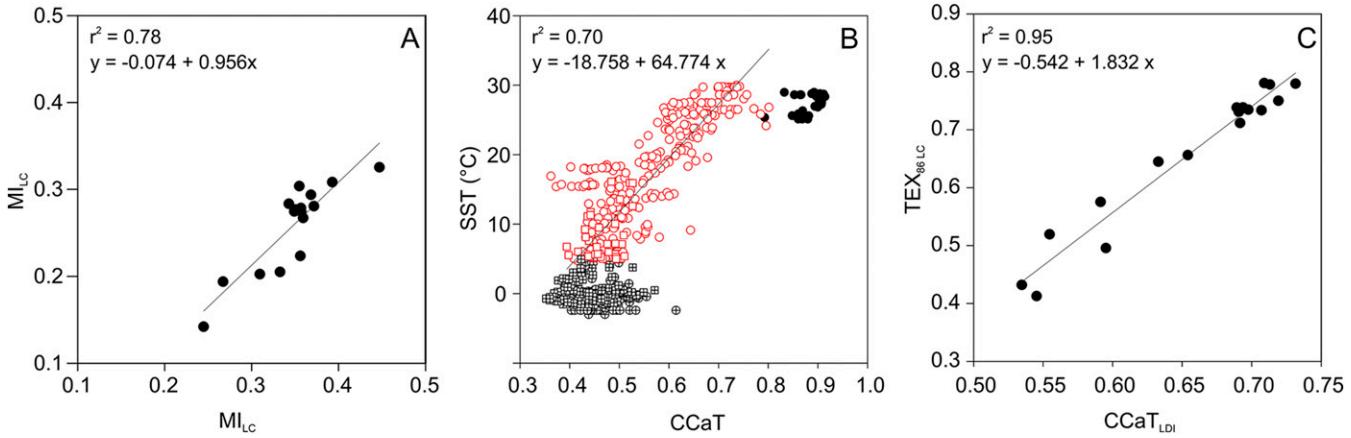

Fig. S5. (*A*) Correlation between MI by LDI FTICR-MS and HPLC/APCI-MS based on 21 sediment samples retrieved during *Meteor* cruise M84-1 (Table S1). (*B*) Correlation of LC-based CCaT from core-top data with satellite-derived SST. Dataset is obtained from Kim et al. (1) (circles) and Ho et al. (2) (squares). As in Kim et al. (1, 3), data from the highly saline Red Sea (black circles) as well as those below 5 °C (crossed symbols) were excluded from the calibration due to large scattering. The five sites in the North Pacific with anomalous GDGT profiles identified by Ho et al. (2) and attributed to methanogenic/methanotrophic activity are neither plotted nor used for calibration. (*C*) Correlation between CCaT by LDI FTICR-MS and TEX_{86} by HPLC/APCI-MS based on 21 sediment samples retrieved during *Meteor* cruise M84-1 (Table S1).

1. Kim J-H, et al. (2010) New indices and calibrations derived from the distribution of crenarchaeal isoprenoid tetraether lipids: Implications for past sea surface temperature reconstructions. *Geochim Cosmochim Acta* 74(16):4639–4654.
2. Ho SL, et al. (2014) Appraisal of TEX_{86} and TEX_{86}^{L} thermometries in subpolar and polar regions. *Geochim Cosmochim Acta* 131:213–226.
3. Kim J-H, Schouten S, Hopmans EC, Donner B, Damste JSS (2008) Global sediment core-top calibration of the TEX_{86} paleothermometer in the ocean. *Geochim Cosmochim Acta* 72(4): 1154–1173.

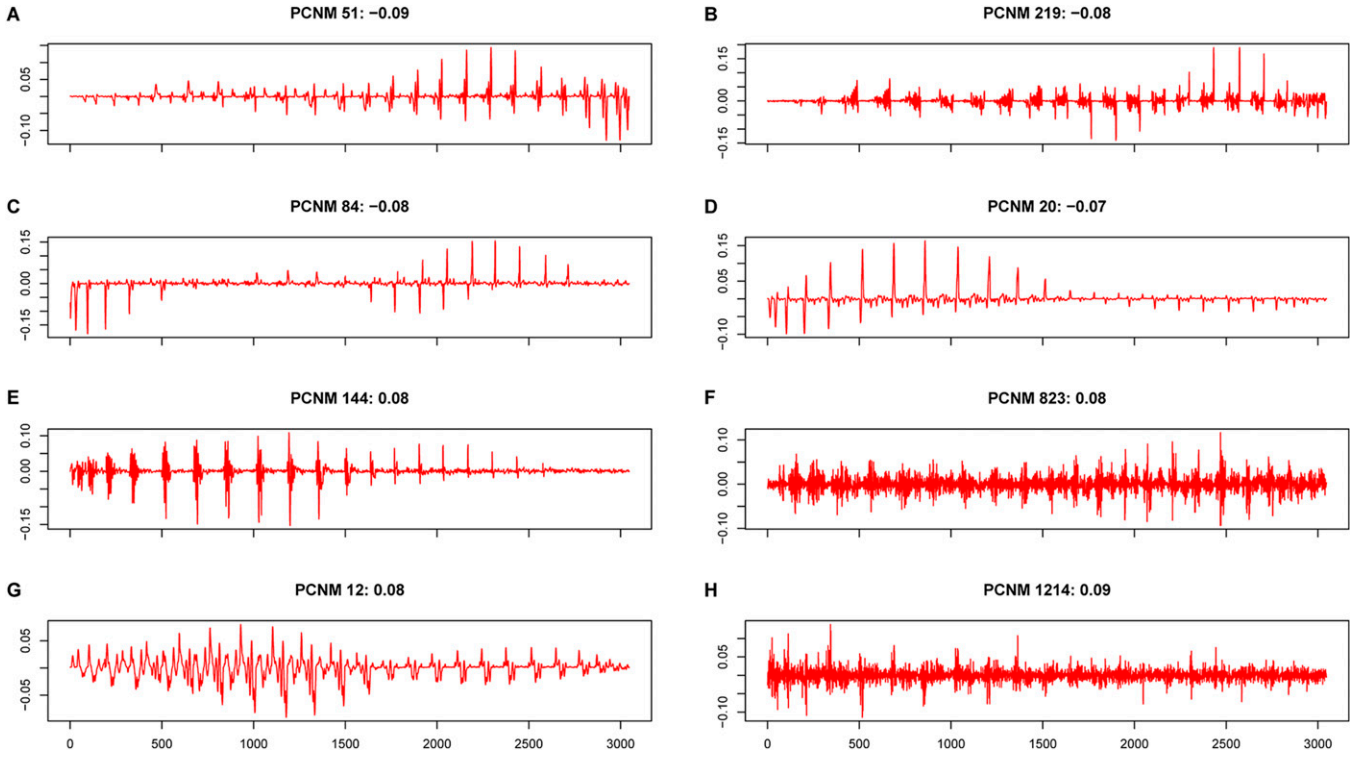

Fig. S6. Illustration of selected PCNM variables generated from the truncated Euclidean distance matrix derived from individual measurement coordinates. Four PCNMs with the greatest absolute negative (*A*–*D*) and positive (*E*–*H*) canonical coefficients (shown above each plot) are displayed and were derived from the pRDA model. The abscissae represent numbered measurements ($n = 3{,}047$) and the ordinates represent the standardized value of the PCNM variable, itself the result of principal coordinates analysis of the truncated distance matrix described above.

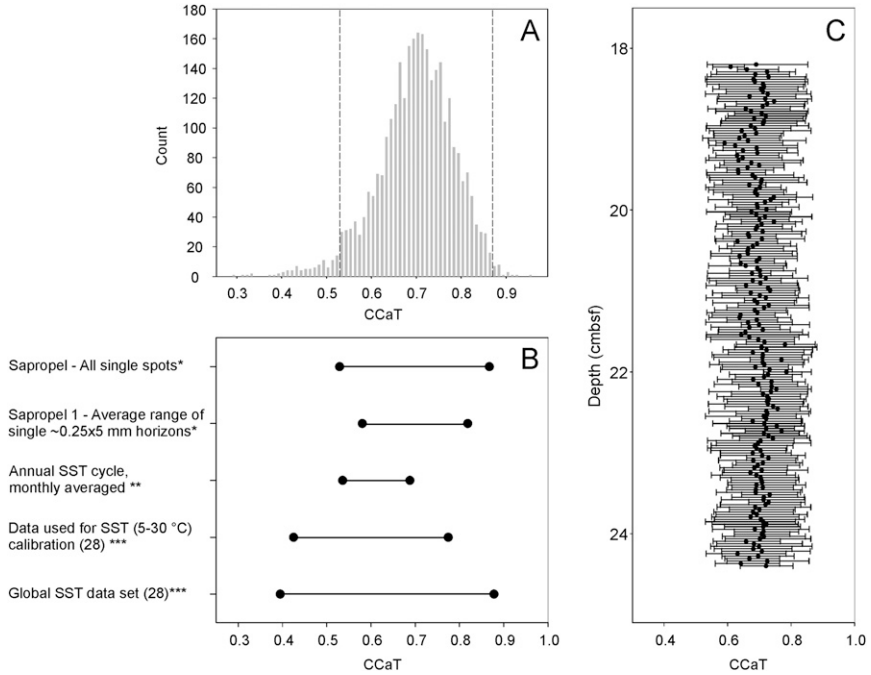

Fig. S7. (*A*) Histogram of single CCaT values corresponding to the high resolution analysis of the 6.2-cm core section from sapropel 1. Vertical dashed line indicates range defined by average ± 2σ. (*B*) Range of CCaT in the sapropel 1 section compared with CCaT ranges derived from annual SST in the modern eastern Mediterranean Sea (1) and from to the global SST data set from Kim et al. (2). *Range of CCaT values in the analyzed sample is defined by mean ± 2σ. **SST values transformed to CCaT (Eqs. **S5** and **S1**) ***Transformed from LC-based values (Eq. **S1**). (*C*) Downcore profile of average values (black solid circles) and corresponding single horizon ranges (horizontal bars) delimited by minima and maxima inside the global mean ± 2σ range from *A*.

1. Kim J-H, et al. (2010) New indices and calibrations derived from the distribution of crenarchaeal isoprenoid tetraether lipids: Implications for past sea surface temperature reconstructions. *Geochim Cosmochim Acta* 74(16):4639–4654.
2. Locarnini RA, et al. (2013) World Ocean Atlas 2013, Volume 1: Temperature. *NOAA Atlas NESDIS 73*, eds Levitus S & Mishonov A (National Oceanographic Data Center, Silver Spring, MD).

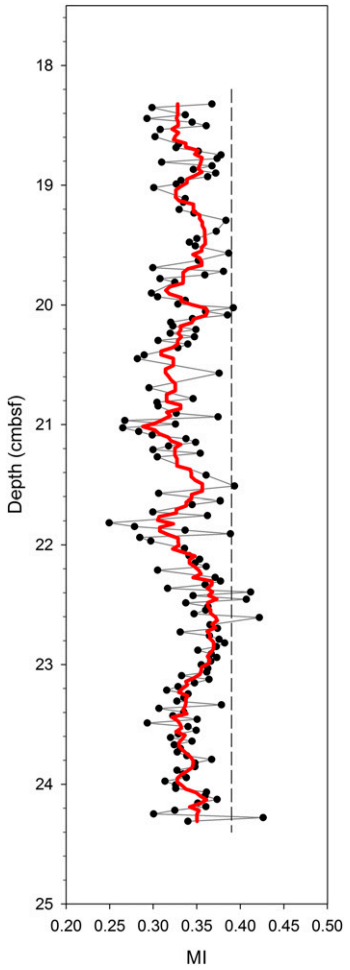

Fig. S8. Downcore profile of MI and seven-point running average (red line). Dashed line at $MI = 0.39$ indicates the threshold for increased methanotrophic activity (17).

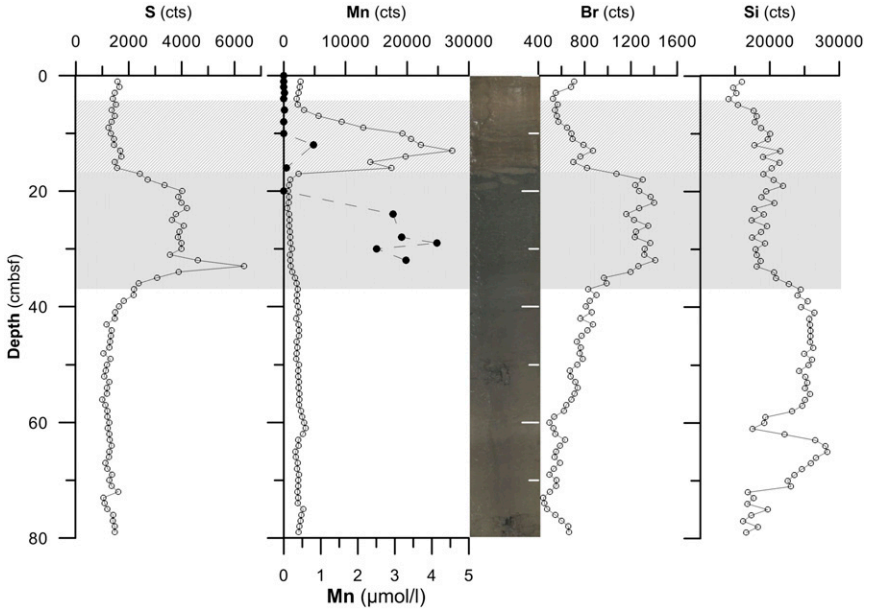

Fig. S9. Downcore profiles of relative element concentrations as detected by XRF scanning (core GeoB 15103-1). Although the data clearly identify the unoxidated part of sapropel 1 between 36 and 17 cmbsf (gray bar), due to oxidation it is hard to detect the total original thickness of the sapropel. The Mn profile indicates that the initial surface may currently be at about 4 cmbsf (dashed area).

Table S1. Characterization of samples retrieved during cruise M84-1 used for validation of GDGT distribution by LDI

Site	Depth (cmbsf)	TOC (wt %)	TN (wt %)	Sedimentology
GeoB 15103 (eastern Mediterranean Sea)	19–39 (12 samples)	1.89	0.13	Sapropel
GeoB 15104 (Marmara Sea)	10–12	1.1	0.12	Coccolith-bearing microcarbonate clay
	180–196	1.03	0.09	Coccolith- and ash-bearing microcarbonate clay
	280–296	n.d.	1.92	Sapropel
	340–355	n.d.	n.d.	Coccolith- and ash-bearing microcarbonate clay
	620–635	0.58	n.d.	Sulfide specks and mottles in carbonate clay
GeoB 15105 (Black Sea)	147–162	1.43	0.14	Clay mixed with diatoms, silt-sized carbonates, siliciclastic material, volcanic ash and coccolithophorides
	390–405	4.37	0.33	Sapropel
	420–435	1.23	0.13	Clay and silt- to sand-sized carbonate clasts, limnic sediment
	596–613	1.12	0.11	Clay and silt- to sand-sized carbonate clasts, sulfide rich

n.d., not determined; TN, total nitrogen; TOC, total organic carbon.

Other Supporting Information Files

Dataset S1 (XLSX)